Predicting the evaporation rate of stationary droplets with the VOF methodology for a wide range of ambient temperature conditions

George Strotos[1,a,*], Ilias Malgarinos[1,b], Nikos Nikolopoulos[1,c], ManolisGavaises[1,d]

[1]School of Engineering and Mathematical Sciences, City University London, Northampton Square, EC1V 0HB, London, UK

[a] George.Strotos.1@city.ac.uk

[b] Ilias.Malgarinos.1@city.ac.uk

[c] Nikolaos.Nikolopoulos.1@city.ac.uk

[d] M.Gavaises@city.ac.uk

[*]Corresponding author

Abstract

This paper presents CFD predictions for the evaporation of nearly spherical suspended droplets for ambient temperatures in the range 0.56 up to 1.62 of the critical fuel temperature, under atmospheric pressures. The model solves the Navier-Stokes equations along with the energy conservation equation and the species transport equations; the Volume of Fluid (VOF) methodology has been utilized to capture the liquid-gas interface using an adaptive local grid refinement technique aiming to minimize the computational cost and achieve high resolution at the liquid-gas interface region. A local evaporation rate model independent of the interface shape is further utilized by using the local vapor concentration gradient on the droplet-gas interface and assuming saturation thermodynamic conditions. The model results are compared against experimental data for suspended droplet evaporation at ambient air cross flow including single- and multi-component droplets as well as experiments for non-convective conditions. It is proved that the detailed evaporation process under atmospheric pressure conditions can be accurately predicted for the wide range of ambient temperature conditions investigated.

Keywords: VOF, evaporation, multi-component, high temperature

1 INTRODUCTION

Droplet evaporation is an important phenomenon realized in several engineering and physical processes; it has been addressed in several textbooks, see selectively [1-4] and review articles [5-8]. Numerical modelling of droplet evaporation started with the idealized evaporation of a spherical, isolated, motionless and constant temperature droplet in an inert gas environment. Under these assumptions, Godsave [9] and Spalding [10] derived the widely known "d^2-law" which predicts that the squared diameter of the droplet reduces linearly with time. Following this approach, these strict assumptions were relaxed by taking into consideration the relative velocity between the air and the droplet, the transient droplet heating, the Stefan flow effects, the evaporation of multicomponent droplets and other secondary phenomena. The transient droplet heating was accounted with the Infinite Conductivity Model (ICM) [11] and the spatial temperature distribution inside the droplet with the Finite Conductivity Model (FCM) [12], the Effective Conductivity Model (ECM) [13] and the parabolic temperature profile model [14]. Regarding the Stefan flow effects which arise from the radial vapor motion, the models of Abramzon & Sirignano [13] and Yao et al. [15] are widely used, while there is a large variety of available heat/mass transfer correlations to account for the relative droplet-gas motion [7]. The performance of the aforementioned models was assessed in comparative studies such as in [16-19].

Modelling of multicomponent droplet evaporation has been also a challenging task since most of the fuels are mixtures of many hydrocarbon components. For a bi-component mixture, the preferential evaporation behavior obeys the distillation behavior of the two components, in which the most volatile species evaporates first followed by the vaporization of the less volatile component. The properties of the mixture depend, in addition to the local temperature, to the concentration. Thus, additional equations need to be solved, accounting for the variation of the species concentration in the liquid phase. Similar to the modelling of the thermal behavior of the droplet, the temporal evolution of the species concentration is simulated by using 0-D or 1-D models, usually known as the Infinite Diffusivity Models (IDM) [20-22] and the Finite Diffusivity Models (FDM) [23-26], respectively.

The aforementioned simplified approaches are suitable for Lagrangian spray models predicting the evolution of sprays plumes in combustion systems, comprised by a large number of polydispersed size droplets, as they do not require a lot of computational resources. On the other hand, their applicability is limited to spherical or near spherical droplets; moreover, they cannot give insight of the complex 3-D fluid and thermal transport processes taking place during

evaporation. Such models require solution of the Navier-Stokes equations along with the energy and species transport equations both for the liquid and gaseous phases simultaneously. The earliest CFD works on droplet evaporation were those of [27-29] who examined the evaporation of single-component spherical droplets and derived useful correlations for the Nusselt and Sherwood numbers, followed later by [30-34]. These works have revealed the importance of the spatial distribution of the velocity, temperature and vapor concentration field and they can be considered as benchmark cases for the validation of 0-D and 1-D models. Later, they were extended to multicomponent fuels in [35-38] and to high pressure conditions in [39]. A common feature of the aforementioned CFD works is that they use a grid fitted to the liquid-gas interface; this provides an accurate representation of the flow field and allows for the determination of the local momentum-heat-mass transfer rates, but they are limited to 2D axisymmetric flows with no or low surface deformation as in [40]. On the other hand, the Volume of Fluid (VOF) and Level Set (LS) methodologies among others can capture the 3D droplet deformation (and even breakup), but with a less accurate prediction of the flow field at the interface region. Recent works on droplet evaporation with the VOF methodology include those of [41-44]. In these works a local evaporation model was used; Schlottke & Weigand [41] used a virtual mass averaged velocity to calculate the source term of the continuity equation at the interface region which improved the model performance. Furthermore, Strotos et al. [42] and Banerjee [43] performed parametric studies for bi-component droplet evaporation while Ghata & Shaw [44] studied the vaporization of fiber-supported droplets and included the effect of thermocapillary stresses at the interface.

The present work examines the droplet evaporation using the solution of the Navier-Stokes equations along with the energy conservation equation, the transport of species and the VOF methodology for tracking the droplet interphase. The validation study examines single- and multi-component droplets for a wide range of ambient temperature conditions under atmospheric pressure. Relative to previous relevant CFD studies with the VOF methodology resolving the complete fluid transport processes during vaporization, including the work of the authors presented in [42], this is one of the first studies (at least to the authors' knowledge) that examines droplet evaporation at temperature ambient conditions above the critical fuel temperature and validates against experimental data the model for a wide range of temperatures. The following sections include the description of the numerical model, the cases simulated, followed by the model predictions for low and high ambient temperature conditions. The conclusions of this work are summarized at the end.

2 MATHEMATICAL MODEL

2.1 Flow field equations

The numerical model involves the solution of the Navier-Stokes equations along with the solution of the transport equation of the liquid phase. The model is an extension of the one used in [45-47] including phase change. In addition, the numerical model employs the Volume of Fluid (VOF) methodology [48] for capturing the droplet liquid-gas interphase. In this methodology, the liquid phase is identified by the liquid volume fraction a_l (defined as the liquid volume in a cell divided by the cell volume) and its transport is given by:

$$\frac{1}{\rho_l}\left[\frac{\partial(a_l\rho_l)}{\partial t} + \nabla\cdot(a_l\rho_l\vec{u}) = -\sum_{\mathrm{k}=1}^{Nsp}\dot{m}'''_{evap,\mathrm{k}}\right] \quad (1)$$

where ρ_l is the liquid phase density, $\vec{u}$ is the velocity vector and $\dot{m}'''_{evap,\mathrm{k}}$ (kg/s/m^3) is the volumetric evaporation rate each of the *Nsp* species composing the liquid phase. The equation (1) can be used for an arbitrary number of phases *Nph* (here *Nph*=2), while the corresponding volume fraction of the gaseous phase can be obtained from the equality a_g=1-a_l. The momentum equations for both phases are written in the form:

$$\frac{\partial(\rho\vec{u})}{\partial t} + \nabla\cdot(\rho\vec{u}\vec{u}) = -\nabla p + \nabla\cdot[\mu(\nabla\vec{u} + \nabla\vec{u}^T)] + \rho\vec{g} + \vec{F}_{vol} \quad (2)$$

where $\vec{F}_{vol}$ is the volumetric force due to surface tension. This is calculated based on the Continuum Surface Force (CSF) approach of Brackbill et al. [49] and it is equal to:

$$\vec{F}_{vol} = \sigma\kappa\vec{n}\frac{\rho}{\frac{1}{2}(\rho_l+\rho_g)} \ , \ \vec{n} = \nabla a \ , \kappa = -\nabla\cdot\left(\frac{\vec{n}}{|\vec{n}|}\right) \quad (3)$$

where σ is the surface tension coefficient, $\vec{n}$ is the normal vector at the interface and κ is the curvature of the interface. Alternatively, the surface tension forces can be included in the momentum equations by using the Continuum Surface Stress (CSS) model by Lafaurie et al. [50] which inherently includes the effects of the variation of the surface tension coefficient along the interface. Equation (4) represents the CSS model, where **I** is the unit tensor and ⊗ is the tensor product of two vectors.

$$\vec{F}_{vol} = \nabla\cdot\left[\sigma\left(|\vec{n}|\mathbf{I} - \frac{\vec{n}\otimes\vec{n}}{|\vec{n}|}\right)\right] \ , \ \vec{n} = \nabla a \quad (4)$$

Additionally, the transport equations for energy, vapor and liquid species concentration are solved:

$$\frac{\partial(\rho E)}{\partial t} + \nabla \cdot [\vec{u}(\rho E + p)] = \nabla \cdot \left[k\nabla T - \sum_{q=1}^{Nph}\left(a_q \sum_{\mathrm{k}=1}^{Nsp} h_{q,\mathrm{k}} \vec{J}_{q,\mathrm{k}}\right)\right] - \sum_{\mathrm{k}=1}^{Nsp} \dot{m}'''_{evap,\mathrm{k}} L_{\mathrm{k}} \quad (5)$$

$$\frac{\partial(a_q \rho_q Y_{q,\mathrm{k}})}{\partial t} + \nabla \cdot \left(a_q \rho_q Y_{q,\mathrm{k}} \vec{u}\right) = \nabla \cdot \left(-a_q \vec{J}_{q,\mathrm{k}}\right) + S_{Y,q} \quad (6)$$

$$\vec{J}_{q,\mathrm{k}} = -\rho_q D_{q,\mathrm{k},m} \nabla Y_{q,\mathrm{k}} \quad \text{, q=gas or liquid} \quad (7)$$

where $\vec{J}_{q,\mathrm{k}}$ is the dilute approximation of the diffusion flux of species k at the mixture of phase q (neglecting the Soret effect), $D_{q,\mathrm{k},m}$ is the diffusion coefficient of kth species in the mixture of phase q (either gas or liquid). Equation (6) is solved in the gas phase (q=gas) for all the vapor species (k=1÷*Nsp*) with a source term equal to $S_{Y,q} = \dot{m}'''_{evap,\mathrm{k}}$. For the case of multicomponent droplets, the same equation is also solved in the liquid phase (q=liquid) for all liquid species with a source term equal to $S_{Y,q} = -\dot{m}'''_{evap,\mathrm{k}}$, except of the main liquid species (k=*Nsp*), since its concentration can be computed from the summation of the liquid species concentrations, which must equal to one.

The properties of the pure components are assumed to be a function of temperature according to [51, 52] and they are updated at every iteration during the numerical solution. The mixture properties (either in the gas or the liquid phase for the case of multicomponent evaporation) follow a mass average rule based on the concentration, while the gas phase density is obtained by assuming incompressible ideal gas.

The numerical settings used for the simulations are: Laminar flow, explicit VOF solution with the Geometric reconstruction scheme [53], Second Order Upwind (SOU) discretization [54] for the momentum and energy equations, First Order Upwind (FOU) for the species transport equations, Body Force Weighted (BFW) pressure interpolation scheme [55], pressure-velocity coupling with the PISO algorithm [56], variable timestep with Courant number *C*=0.25 both for the interface tracking and the whole computational domain (global Courant number).

The commercial CFD code ANSYS FLUENT v14.5 [55] has been utilized for the solution of the flow equations with a number of user defined functions (UDF) for resolving the above processes; more specifically, UDFs have been used for applying the automatic local grid refinement technique and the interface sharpening algorithm [47] required to minimize the interface diffusion which is promoted by the evaporation source terms. Moreover, the evaporation rate model described in the next section is also implemented using UDF together with the functions addressing the fluid, vapor and gas properties as function of local temperature [51, 52].

2.2 Evaporation rate model

The evaporation rate is calculated as in [42, 43, 57, 58] by applying the simplified Fick's law at the liquid-gas interface cells:

$$\dot{m}''_{evap,\mathrm{k}} = \rho_g D_{g,\mathrm{k},m} \left(\frac{dY_{g,\mathrm{k}}}{dn}\right)_{surf} \quad , \mathrm{k}=1 \div Nsp \tag{8}$$

The evaporation source term $\dot{m}'''_{evap,\mathrm{k}}$ is obtained by multiplying equation (8) with $A_{l,cell}/V_{cell} = |\nabla a|$. The evaporation rate of equation (8) is independent of the interface shape and does not require any reference length or velocity. Although it is based on a diffusion law, the flow conditions are taken into account through the solution of the Navier-Stokes equations which advect the vapor and modify the local concentration gradient. Besides this simplified Fick's law, a more physically correct expression was also examined which takes into consideration the Stefan flow:

$$\dot{m}''_{evap,\mathrm{k}} = \frac{\rho_g D_{g,\mathrm{k},m} \left(\frac{dY_{g,\mathrm{k}}}{dn}\right)_{surf}}{1 - Y_{g,\mathrm{k},sat}} \tag{9}$$

Equation (9) has been used in Schlottke & Weigand [41] among others and it is valid only for single-component evaporation. For multi-component evaporation, the exact expression for the evaporation rate was given in Renksizbulut & Bussmann [38] but it was not examined here since it is more complicated and computationally expensive. For low evaporation rates and when the droplet temperature is not close to the boiling temperature (i.e. small Spalding numbers, $B_M << 1$), both expressions are valid.

The key parameter in the implementation of the evaporation rate model is the calculation of the concentration gradient magnitude $(dY_g/dn)_{surf}$. The interfacial cells are assumed to be saturated and the vapor saturation concentration Y_{sat} is calculated as a function of the cell temperature (and liquid composition when multicomponent evaporation is examined). An algorithm is used to identify the closest neighbor cell (subscript ∞) to the direction of the normal vector of the interface $\vec{n}$; this is illustrated in Fig. 1. Denoting as $\vec{d}$ the vector connecting the two cells, two options exist for the calculation of the concentration gradient (see details in Fig. 1) in non-orthogonal unstructured grids. The first one is the simplest but less accurate when the vectors $\vec{n}$ and $\vec{d}$ are not aligned. The second one is more accurate since it accounts for the angle between the two vectors; it works for all types of grid and it is the default method in the present model.

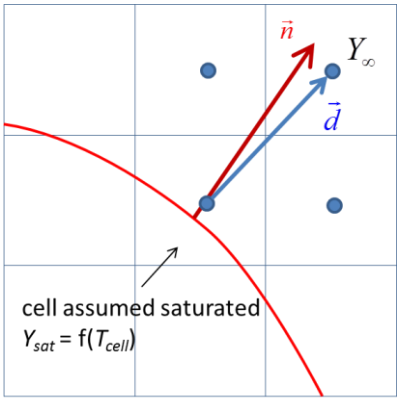

1. $$\left(\frac{dY_g}{dn}\right)_{surf} = \frac{Y_{sat} - Y_\infty}{|\vec{d}|}$$

2. $$\left(\frac{dY_g}{dn}\right)_{surf} = \frac{Y_{sat} - Y_\infty}{|\vec{d}|}\frac{\vec{d}}{|\vec{d}|}\cdot\frac{\vec{n}}{|\vec{n}|}$$

Fig. 1: Illustration of the two different methods employed for the estimation of the vapor concentration gradient at the liquid-gas interface. The 2nd method has been finally adopted in the present work.

Finally, the vapor diffusion coefficient $D_{g,\mathrm{k},m}$ of the kth species in the gas mixture, is obtained by using the dilute approximation (Eq. 10), in which $X_{g,k}$ is the mole fraction of species k in the gas phase and $D_{g,\mathrm{i,j}}$ is the binary diffusion coefficient of species i in species j; the latter is a function of temperature:

$$D_{g,k,m} = \frac{1 - X_{g,k}}{\sum_{j,j\neq i}(X_{g,j}/D_{g,i,j})} \quad (10)$$

3 DESCRIPTION OF THE TEST CASES SIMULATED

The mathematical model used is validated against 3 sets of experimental data for suspended droplet evaporation for: (a) convective air flow conditions (experimental data of Daïf et al. [59]), (b) the data of Wong & Lin [60] and (c) under microgravity conditions in a quiescent gas environment (experimental data of Nomura et al. [61]). The cases examined are presented in Table 1; they all refer to atmospheric ambient pressure. As it can be seen, they cover a wide range of conditions including single- and multi-component evaporation, sub- and super-critical gas temperature conditions, low and moderate *Re* numbers, as also species with a large volatility difference (n-heptane and n-decane). More specifically, cases 1-3 correspond to the experimental data of Daïf et al. [59] who examined droplet evaporation at low temperature conditions and moderate *Re*

numbers for droplets consisting of n-heptane (case 1), n-decane (case 2) and a mixture of the two with 74% n-heptane (case 3). Case 4 corresponds to the experimental data of Wong & Lin [60] who examined the evaporation of n-decane droplets in a high temperature gas environment and low Re number flow. Cases 5-8 correspond to the experimental data of Nomura et al. [61], who investigated suspended n-heptane droplets in high temperature ambient conditions. Each set of the aforementioned experimental data is examined in a separate section in the present paper, in which the experimental and the numerical setup are presented in detail.

Table 1: Experimental conditions examined

case	species	d_0 [mm]	$T_{d,0}$ [K]	T_∞ [K]	u_∞ [m/s]	Re_0	ref
1	C7	1.052	300	356	3.20	159	[59]
2	C10	1.386	315	348	3.10	210	[59]
3	C7-C10 74-26%	1.334	294	348	3.10	203	[59]
4	C10	1.961	315	1000	1.0	17	[60]
5	C7	0.700	300	471	~ 0	~ 0	[61]
6	C7	0.700	300	555	~ 0	~ 0	[61]
7	C7	0.700	300	648	~ 0	~ 0	[61]
8	C7	0.700	300	741	~ 0	~ 0	[61]

4 RESULTS & DISCUSSION

4.1 Evaporation at low temperature conditions. Experimental data of Daïf et al. [59]

In this section the numerical model is validated against the experimental data reported in Daïf et al. [59] for cases 1-3 of Table 1. These refer to subcritical ambient temperature conditions and include the evaporation of single- and multicomponent droplets at moderate *Re* numbers. In [59] the droplets were held in suspension at the spherical head of a capillary tube (400 and 200μm respectively), which was placed perpendicularly to the gas flow. They used a video camera to record the droplet diameter and an infrared thermo-graphic system to measure the droplet's surface temperature.

The computational domain, the boundary conditions and the grid used for these cases are shown in Fig. 2a; they are similar to these used in Strotos et al. [42]. The flow was assumed to be 2D-axisymmetric since the *Re* number is below 400 for all cases examined and the presence of the capillary tube is not expected to induce 3D effects. The spherical head of the suspender was assumed to be an adiabatic impermeable wall and the liquid contact angle was set to 10 degrees as in [42]. Regarding the initial conditions, uniform velocity, temperature and concentration fields were assumed. The grid used is unstructured with 2 levels of adaptive local refinement; this is based on the work of Theodorakakos & Bergeles [62] and implemented here as in Malgarinos et al. [45]. A grid independent solution is achieved by using 2 levels of local grid refinement as shown in Fig. 2b for the prediction of the dimensionless droplet volume temporal evolution. This is a good compromise between accuracy and computational cost which is approximately 1.7CPU-days for each second of physical time for the single-component cases and 2.3CPU-days/sec for the bi-component evaporation case.

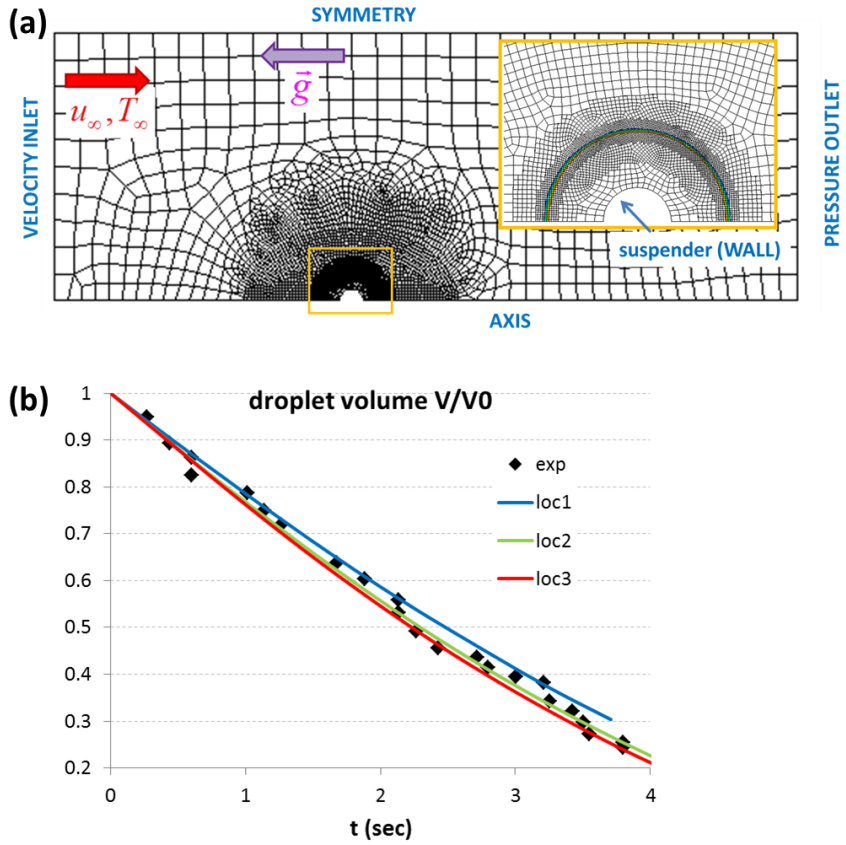

Fig. 2: (a) Computational domain and boundary conditions employed. The inset figure shows the grid topology around the liquid-gas interface for two levels of adaptive local grid refinement. (b) Temporal evolution of droplet's non-dimensional volume for the case 1 using one-, two- and three-levels of local grid refinement.

The temporal evolution of the non-dimensional droplet squared diameter and the mean droplet temperature for the cases of Daïf et al. [59] are presented in Fig. 3a and Fig. 3b, respectively. The predictions are in good agreement with the experimental data regarding the droplet size, while the wet-bulb temperature of n-decane is overestimated by 4°C; this is within the accuracy of previously published studies for the same case [25, 42, 63, 64]. Single-component droplets (cases 1 and 2) after an initial heat-up period follow the d^2-law and they reach the wet-bulb temperature corresponding to the experimental conditions. The two-component droplet (case 3) exhibits preferential evaporation in which the more volatile n-heptane evaporates first and then the less volatile n-decane follows. The relevant physical processes during the multicomponent evaporation have been discussed in depth discussed in Strotos et al. [42, 65].

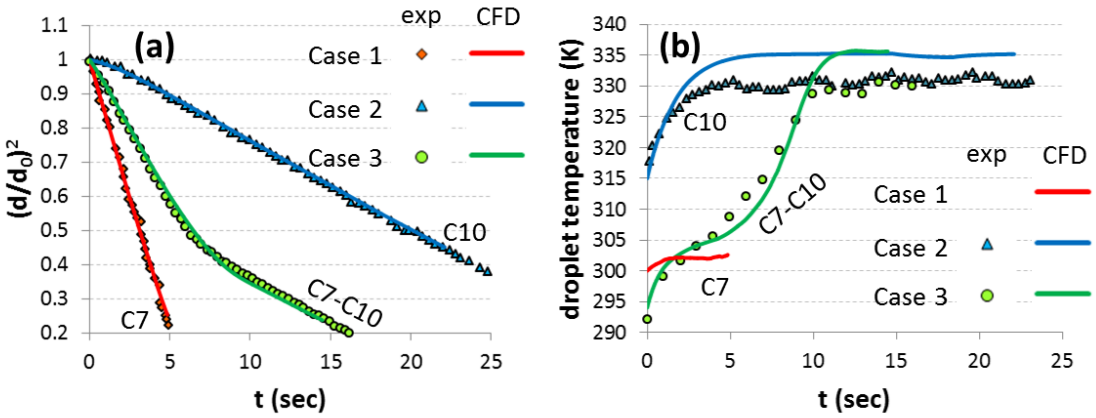

Fig. 3: Model predictions for the experimental data of Daïf et al. [59]. Temporal evolution of (a) droplet size and (b) mean droplet temperature. No experimental data were provided for the droplet temperature in case 1.

Initially, the spherical suspender lies at the centre of the droplet; under the action of gravitational and aerodynamic forces the droplet moves either upwards or downwards as shown in Fig. 4. The n-heptane droplet (case 1) is relatively light and moves upwards (opposite to the direction of gravity in Fig. 4), while the droplets of the other two cases are heavier and they move initially downwards (in the direction of gravity in Fig. 4). As the droplet evaporates and becomes lighter, the gravitational force become smaller compared to the aerodynamic one and the droplet progressively moves to the other side of the suspender. After reaching an equilibrium position, the droplets are held in touch with the suspender due to the adhesion forces. Behind the droplet, a large recirculation zone appears and its length is plotted versus the gas phase *Re* number in Fig. 5; the experimental data of Taneda [66] for a solid sphere are also shown. The wake length increases with increasing *Re* number and it is slightly restricted compared to the one formed under the same flow conditions behind a solid sphere. This is attributed to the liquid phase recirculation which moves the flow separation point towards the rear of the droplet and suppresses the length of the wake, as also reported previously in Sirignano [2].

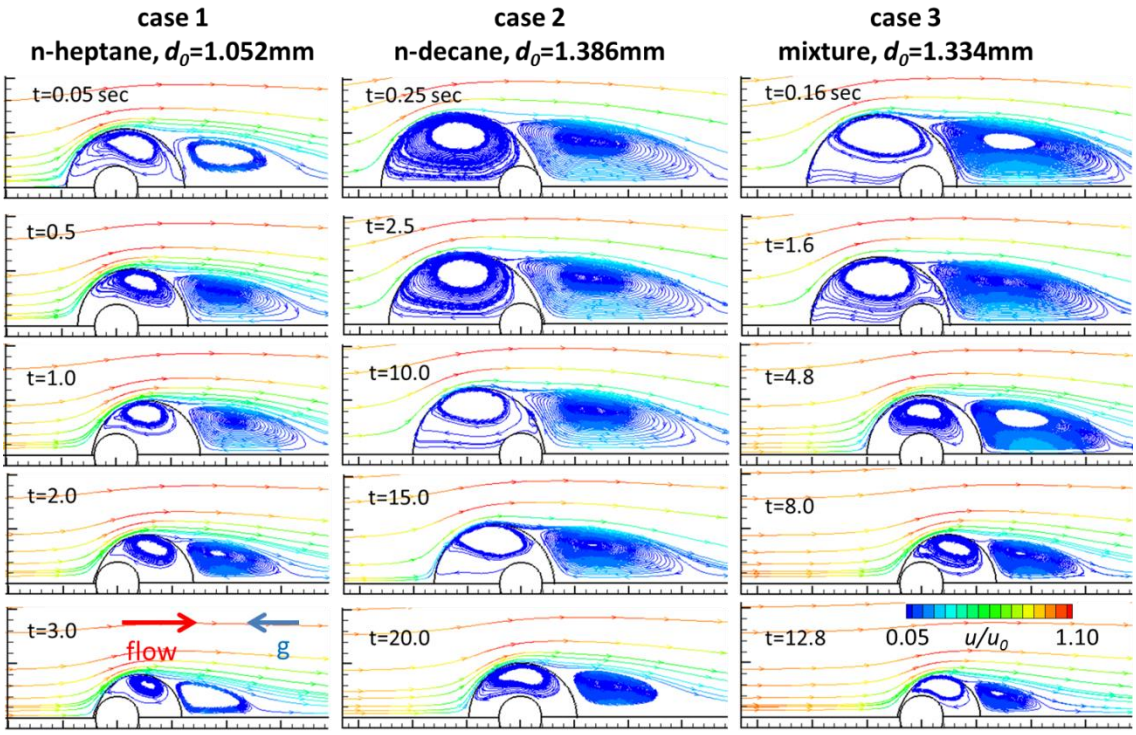

Fig. 4: Predicted transient droplet motion and flow field streamlines for the experiments of Daïf et al. [59] (cases 1-3).

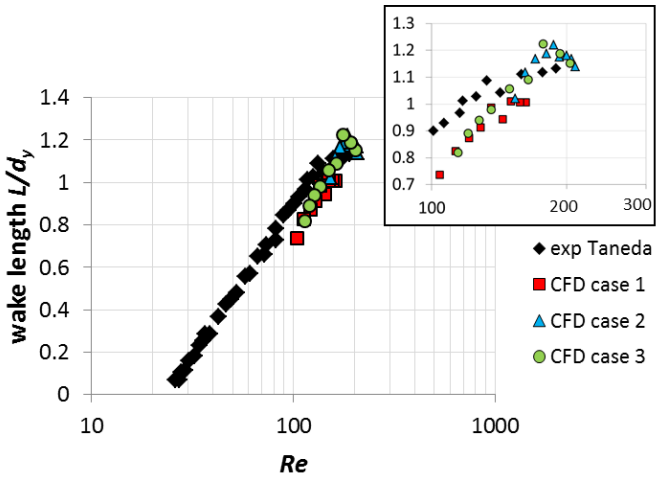

Fig. 5: Dependence of the wake recirculation length with the *Re* number for cases 1-3.

In Fig. 6 representative velocity, temperature and vapor fields are presented for the n-decane case at 0.25 and 20.0sec; the velocity field is depicted by the streamlines colored with the velocity magnitude. The spatial distribution of the temperature and the vapor field is influenced by the recirculation zones formed inside and behind the droplet, as also the presence of the solid suspender. Inside the droplet, a relatively cooler region is identified at the vortex core (as also

observed in [29, 30]), while at the wake behind the droplet the temperature and the vapor concentration fields are similar between them and they are influenced by the gas phase vortex.

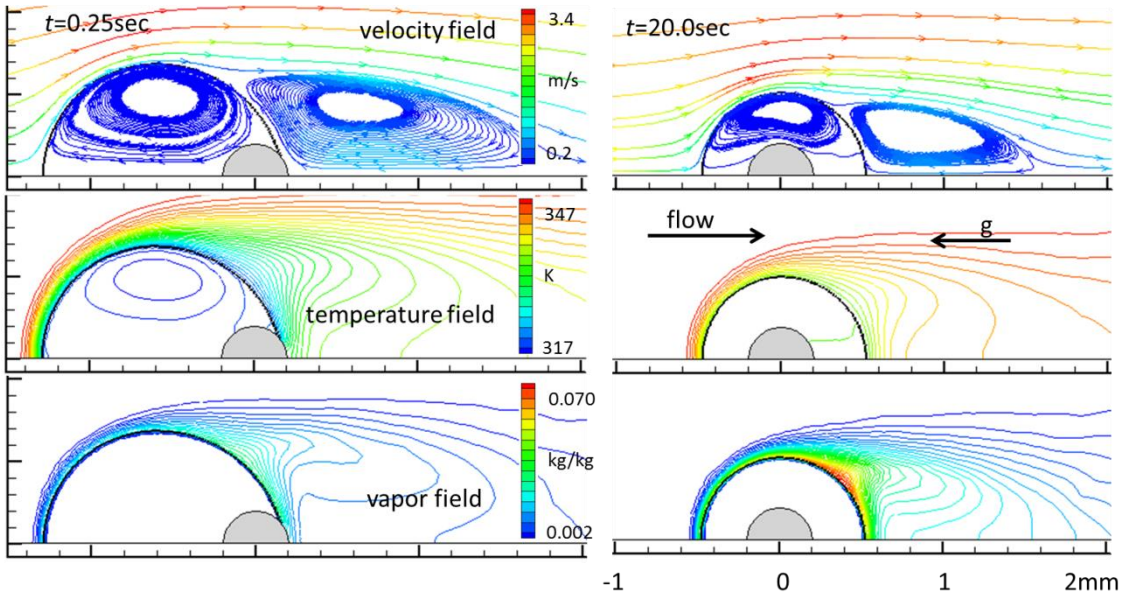

Fig. 6: Velocity streamlines, temperature and vapor concentration field for the n-decane droplet (case 2).

In Fig. 7 the spatial distribution of the evaporation source term (in kg/m^{3}s) at selected time instances is presented for the n-decane droplet; the non-interpolated contours shown correspond to the region between VOF values equal to 0.01 and 0.99. As it can be seen, there is a narrow region at the interface (2-3 cells) in which the evaporation source term is distributed and it maximizes near the 0.5 iso-VOF line, in which the quantity $|\nabla a|$ maximizes too (see also the inset figure at t=20sec). The thickness of this region in length units depends on the grid density, but it has a minor effect on the overall evaporation process, as shown in Fig. 2b. The evaporation rate increases with time, since the droplet temperature also increases; it is interesting to observe that the maximum evaporation rate is observed around 30-40^o away from the front stagnation point, which was also observed in Shih & Megaridis [31]. The minimum evaporation rate is observed near the point of flow separation at approximately 130-140^o; this behavior was also observed in Haywood et al. [28]. The spatial distribution of the evaporation rate is not smooth and this is ought to the imperfect distribution of the VOF values over the computational cells.

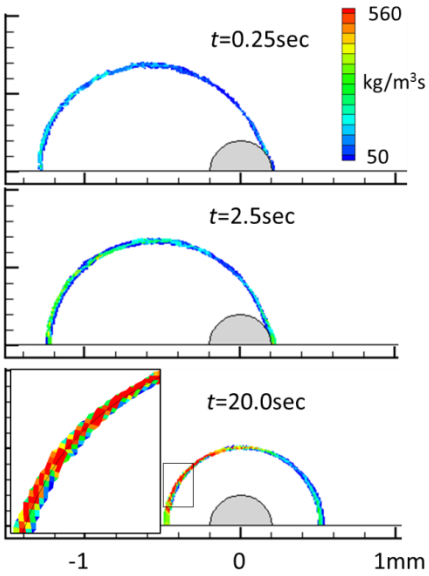

Fig. 7: Spatial distribution of the evaporation rate at different time instances for the n-decane droplet (case 2).

One of the parameters examined was the effect of the thermo-capillary flow (Marangoni effect) induced by the variation of the surface tension coefficient along the interface. This is achieved by using the CSS formulation [50] instead of the CSF model [49] in order to calculate the surface tension forces in the momentum equations. As it was also shown in Strotos et al. [42], the temperature along the interface does not exhibit large variations and the Marangoni effect does not affect the droplet evaporation for these specific cases. On the other hand, it seems to create a kind of unsteadiness by increasing the fluctuations of the droplet shape but without a noticeable effect on the liquid phase internal circulation; unsteadiness in thermo-capillary flows were also observed in Shih & Megaridis [32]. The single-component cases 1-2 were also examined by using the evaporation rate of equation (9). The results have shown that it has a negligible effect on the prediction of the phenomenon due to the low evaporation rate and thus it is not presented.

4.2 Evaporation at high temperature conditions. Experimental data of Wong & Lin [60]

The 4th case of Table 1 corresponds to the experimental data of Wong & Lin [60] who examined the evaporation of n-decane droplets in a supercritical gas environment (T_∞= 1000K, $T_{cr,C7}$=617.7K). The droplet was suspended at a ceramic shell attached to a 100μm glass filament; the droplet internal temperature distribution was measured by using thermocouples (25μm wire diameter and ~70μm bead diameter) placed at different positions inside the droplet.

This set of experimental data has been widely used in validation studies for 0-D and 1-D models [16, 19, 63, 67, 68] as also in CFD studies by [30, 33], which assumed a spherical droplet shape and neglected the presence of the shell-like suspender. In the present study the presence of the suspender has been considered but assumed to be spherical since its exact geometry and dimensions were not reported in the relevant paper.

The model predictions for the droplet size and the mean droplet temperature are shown in Fig. 8 by using the two variations of the evaporation model described in section 2.2, i.e using equation (8) and (9), respectively. The predictions for the droplet size are satisfactory for both models with the second one having a slightly higher evaporation rate at the beginning and lower at subsequent times. In both cases the droplet's size regression deviates significantly from the d^2-law due to the intense and long droplet heat-up period. During this period, the thermal expansion of the droplet is more intense compared to the droplet evaporation and the droplet size slightly increases; this phenomenon has been observed in [39, 69] among others. Regarding the model predictions for the droplet temperature, the available experimental data for the droplet temperature were obtained by placing three thermocouples at fixed positions (r/R_0=0, ±0.6). Such information was difficult to be obtained with the current numerical setup since the droplet moves over the suspender and also deforms. So, in Fig. 8 the model prediction for the mean droplet temperature is presented, which is closely related to the measured quantities. The temperature prediction is in accordance with the experimental measurements but this time the simplified Fick's model of eq (8) has a better performance predicting accurately the wet-bulb temperature. The present results are within the accuracy of the results obtained with other numerical methodologies mentioned at the beginning of this section. It has to be noted that at the latter stages of evaporation, the interface diffusion problems associated with the VOF methodology become more pronounced and are more intense for high evaporation rates; this explains why the droplet temperature predicted with equation (9) further increases for t>2.5sec.

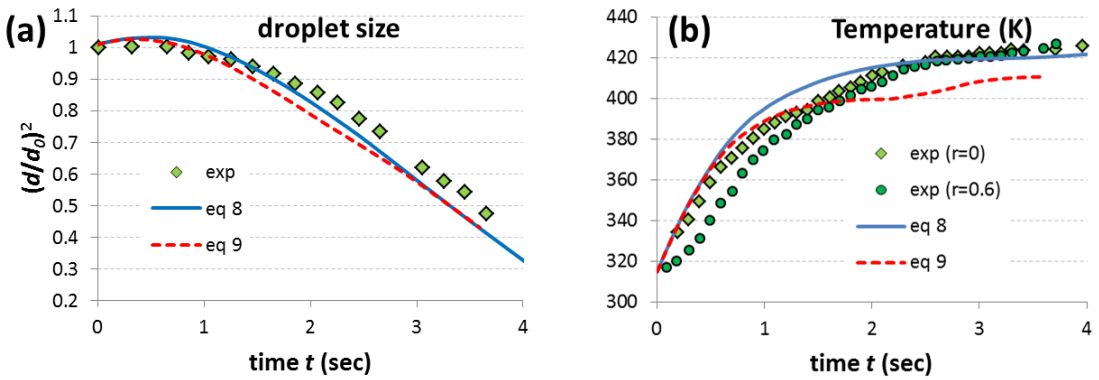

Fig. 8: Model predictions for the experimental data of Wong & Lin [60]. (a) temporal evolution of droplet size and (b) mean droplet temperature.

The predicted flow, temperature and vapor concentration field for the experimental case of [60] are shown in Fig. 9. The gravitational forces are quite strong and the droplet moves downwards to the direction of gravity. Since the *Re* number of the flow is below 20, there is no recirculation in the gas phase downwind the droplet and the temperature and vapor concentration fields have a slightly different topology compared to the cases 1-3 presented in the previous section 4.1. Furthermore, the thickness of the temperature and concentration boundary layers seem to be higher compared to those of cases 1-3 and this ought to the fact that the boundary layer thickness is proportional to $(RePr)^{-1/2}$ [70] as also to the thickening of the boundary layer due to the intense evaporation rate [19].

Inside the droplet, the liquid circulation is quite disturbed forming two unsteady vortices which tend to homogenize the temperature. This is in contradiction with the experimental observations of Wong & Lin [60] as also with the numerical solution of Megaridis [30]. The inability to capture this phenomenon in the current work is probably ought to the parasitic velocities induced by the VOF methodology [71, 72], which originate from the imbalance between surface tension and pressure gradient forces. The case examined has a low *Re* number and the parasitic velocities become important while they are further magnified due to the high density ratio between the liquid and the gas phase, which exceeds 2000 in this case. Nevertheless, the overall behavior of droplet evaporation is not affected by the spurious currents and the experimental data are correctly predicted. In an effort to reduce the magnitude of these velocities, several options were examined, such as reducing the computational time-step down to a Courant number of 0.1, increasing the smoothing iterations of VOF function and using different discretization schemes for the VOF; however, none of these methods could improve the predicted velocity field. The unphysical velocities could be potentially minimized by applying the algorithm described in Francois et al. [72], but the pressure-velocity coupling in FLUENT is hardcoded and cannot be modified as stated in [73]. The CSS surface tension scheme was also examined, but the induced thermo-capillary flow along with the spurious velocities resulted in high deformation of the droplet shape. Thus, the CSS simulations are not considered accurate and they are not presented.

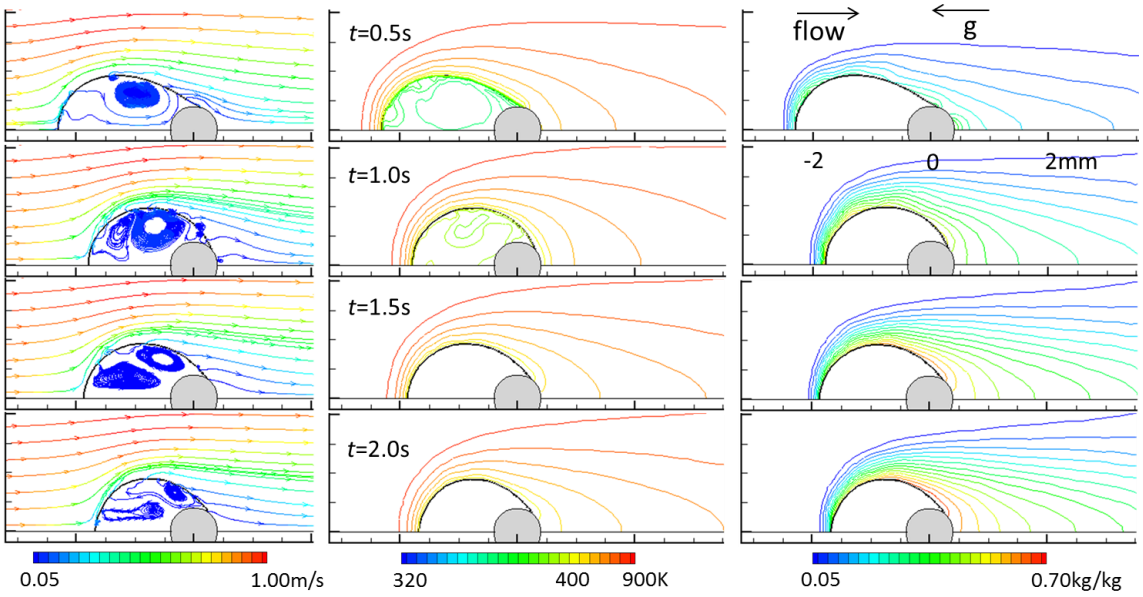

Fig. 9: Predicted flow field streamlines, temperature and vapor concentration field for the experimental case of Wong & Lin [60].

4.3 Evaporation at high temperature conditions. Experimental data of Nomura et al. [61]

Cases 5-8 of Table 1 correspond to the experimental data of Nomura et al. [61], who examined the evaporation of suspended n-heptane droplets for a wide range of ambient temperature and pressure conditions; these data have been widely used to validate 0-D and 1-D models (see [18, 39] among others). The experiments were conducted at microgravity conditions to prevent the natural convection and the vapor was flowing radially as stated in Nomura et al. [61]. The droplet diameters examined were in the range 0.6-0.8mm but the exact values were not reported. However, as the time axis of their plots was presented as t/d_0^2 this normalization results to the prediction of vaporization time independent on the selection of the droplet diameter. In the present work, a diameter of 0.7mm was selected as the mean among the experimental values. Regarding the initial droplet temperature, a value of 300K was used. Simulations of the cases of [61] were simplified by disabling the solution of the flow equations and accounting only for the transient and the diffusion terms in the conservation equations. This selection is justified by the fact that the velocities are quite low and the vapor flows radially [61]. Note that this is not equivalent to a 1-D model which assumes spherical symmetry, since a 2-D computation domain is used (Fig. 10) and the grid cells are not aligned with the liquid-gas interface (see inset figure in Fig. 10). More importantly, the gas phase temperature and concentration are also solved, so there is no need to estimate "film" gas properties near the interface, as also the Nusselt and

Sherwood numbers are not a-priori assumed, but become a part of the solution through the predicted temperature and vapor concentration gradients. It has also to be noted that this approach is not applicable in the experiments examined in the previous sections, since the gas phase velocity plays a dominant role. The grid used is shown in Fig. 10 and it represents an adiabatic box extended $25d_0$ far from the droplet. The box dimensions are large enough so that the average gas temperature remains practically constant.

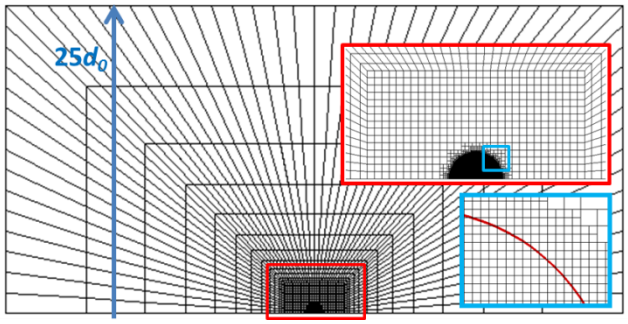

Fig. 10: Numerical grid used for the experimental data of Nomura et al. [61].

The model results for the dimensionless squared droplet diameter are shown in Fig. 11a for the four different ambient temperatures examined. As it can be seen, the model results are satisfactory for a wide range of ambient temperatures even above the critical one ($T_{cr,C7}$=540.2K). The droplet evaporation rate is shown in Fig. 11b. The evaporation rate increases at the initial stages of the evaporation due to droplet heat up and after reaching a maximum it decreases due to the reduction of the droplet surface area. This behavior is observed in all cases and it generally increases with increasing ambient temperature.

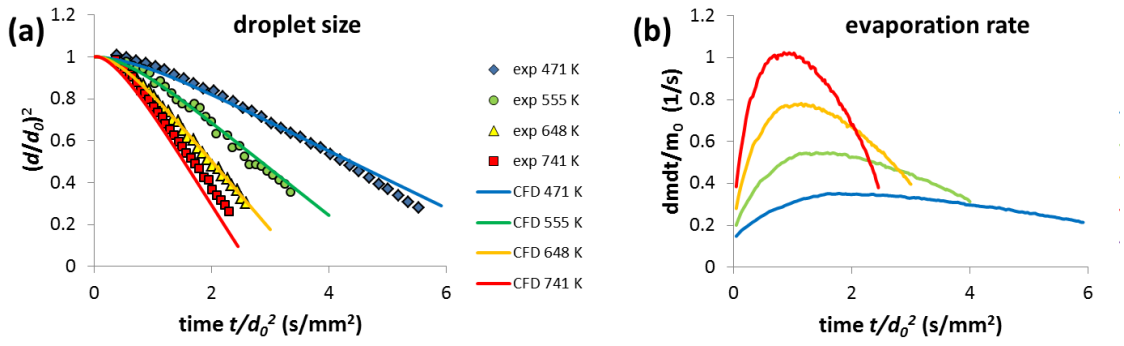

Fig. 11: Model predictions for the experimental data of Nomura et al. [61]. (a) temporal evolution of droplet size and (b) evaporation rate.

5 CONCLUSIONS

The Navier-Stokes equations coupled with the conservation equations for energy and species concentration and the VOF methodology were used to study the evaporation of suspended single- and multi-component droplets. The local evaporation rate was estimated by using the Fick's diffusion law, which is independent of the interface shape and grid density. The model performance was assessed by comparing the results against experimental data for single- and bi-component fuel droplets under sub- and super-critical ambient temperature conditions. Prediction of the overall evaporation rate for a wide range of cases was satisfactory, while prediction of the droplet's temperature was within the accuracy of other published works. For the cases with *Re* of O(100) the recirculation zones at the gas and the liquid phase are correctly predicted and agree with the numerical solutions from other researchers. For the case with *Re* of O(10), the model could not capture the liquid phase internal recirculation zone since the parasitic velocities induced by the VOF methodology were large compared to the flow velocity. Overall, the numerical model can be considered as a reliable tool able to predict the lifetime and temporal evolution of droplet evaporation in a wide range of ambient temperature conditions for moderate and high Re numbers. In comparison to simplified (but also faster) 0-D and 1-D models, the present model gives insight into the spatial distribution of the flow variables and more importantly, it can be extended without any modification to predict the evaporation of deformed droplets and droplets undergoing breakup; see [74]. Nevertheless, with the today's computational resources, the present model cannot be used to simulate sprays comprised by a large number of droplets.

6 ACKNOWLEDGEMENTS

The research leading to these results has received funding from the People Programme (Marie Curie Actions) of the European Union's Seventh Framework Programme FP7-PEOPLE-2012-IEF under REA grant Agreement No. 329116.

7 NOMENCLATURE

Symbol	Quantity	SI Unit
A	Surface area	m^2
B_M	Spalding number $B_M = (Y_{g,sat} - Y_{g,\infty})/(1 - Y_{g,sat})$	-
c_p	Specific heat capacity	J/(kg·K)
d	Diameter	m
$\vec{d}$	Vector connecting adjacent cells	m
D	Mass diffusion coefficient	m^2/s
E	Specific internal energy	J/kg
F	Force	N
g	Gravity acceleration	m/s^2
h	Specific enthalpy	J/kg
$\mathbf{I}$	Unit tensor	-
$\vec{J}_{q,\mathrm{k}}$	Species flux	kg/m^2s
k	Thermal conductivity coefficient	W/(m·K)
L	Latent heat of vaporization	J/kg
$\dot{m}''$	Evaporation rate	kg/m^2s
$\dot{m}'''$	Evaporation source term	kg/m^3s
n	Normal coordinate to gas-liquid interface	-
Nph	Total number of phases	-
Nsp	Total number of liquid species	-
p	Pressure	N/m^2

Pr	Prandtl number	-
R	Radius	m
r	Coordinate in radial direction	m
Re	Reynolds number $Re = \rho_{g,\infty} d_0 u_\infty / \mu_{g,\infty}$	-
S	Source term	
T	Temperature	K
t	Time	s
u	Velocity	m/s
V	Volume	m^3
x,y,z	Coordinates	m
Y	Mass concentration	kg/kg

Greek Symbols

Symbol	Quantity	SI Unit
α	Liquid volume fraction	-
κ	Curvature	m^{-1}
μ	Viscosity	kg/(m·s)
ρ	Density	kg/m^3
σ	Surface tension coefficient	N/m

Subscripts

Symbol	Quantity
0	Initial
∞	Conditions far from the droplet

cell	Cell
cr	Critical
d	Droplet
evap	Evaporation
exp	Experimental
g	Gas phase
k	k^{th} species of the mixture
l	Liquid phase
m	Mixture
mean	Mean
q	of phase q
sat	Saturated
surf	Surface interface
vap	Vapor

abbreviations

C10	n-decane
C7	n-heptane
CSF	Continuum Surface Force
CSS	Continuum Surface Stress
ECM	Effective Conductivity Model
FCM	Finite Conductivity Model
FDM	Finite Diffusivity Model
ICM	Infinite Conductivity Model

IDM	Infinite Diffusivity Model
VOF	Volume Of Fluid

8 REFERENCES

[1] Clift R., Grace J.R., Weber M.E., Bubbles, drops and particles, Academic Press, New York, 1978.

[2] Sirignano W.A., Fluid Dynamics and Transport of Droplets and Sprays, Cambridge University Press, 1999.

[3] Bird R.B., Stewart W.E., Lightfoot E.N., Transport Phenomena, 2nd ed., Wiley, New York, 2002.

[4] Asano K., Mass Transfer – from Fundamentals to Modern Industrial Applications, Wiley VCH Verlag GmbH & Co. KGaA, Weinheim, Germany, 2006.

[5] Givler S.D., Abraham J., Supercritical droplet vaporization and combustion studies, Progress in Energy and Combustion Science, 22 (1996) 1-28.

[6] Bellan J., Supercritical (and subcritical) fluid behavior and modeling: drops, streams, shear and mixing layers, jets and sprays, Progress in Energy and Combustion Science, 26 (2000) 329-366.

[7] Sazhin S.S., Advanced models of fuel droplet heating and evaporation, Progress in Energy and Combustion Science, 32 (2006) 162-214.

[8] Erbil H.Y., Evaporation of pure liquid sessile and spherical suspended drops: A review, Advances in Colloid and Interface Science, 170 (2012) 67-86.

[9] Godsave G.A.E., Burning of Fuel Droplets in: 4th International Symposium on combustion, The Combustion Institute, Baltimore, 1953, pp. 818-830.

[10] Spalding D.B., The combustion of liquid fuels, in: 4th International Symposium on combustion, The Combustion Institute, Baltimore, 1953, pp. 847-864.

[11] Law C.K., Unsteady droplet combustion with droplet heating, Combustion and Flame, 26 (1976) 17-22.

[12] Law C.K., Sirignano W.A., Unsteady droplet combustion with droplet heating--II: Conduction limit, Combustion and Flame, 28 (1977) 175-186.

[13] Abramzon B., Sirignano W.A., Droplet vaporization model for spray combustion calculations, International Journal of Heat and Mass Transfer, 32 (1989) 1605-1618.

[14] Dombrovsky L.A., Sazhin S.S., A parabolic temperature profile model for heating of droplets, Journal of Heat Transfer, 125 (2003) 535-537.

[15] Yao G.F., Abdel-Khalik S.I., Ghiaasiaan S.M., An Investigation of Simple Evaporation Models Used in Spray Simulations, Journal of Heat Transfer, 125 (2003) 179-182.

[16] Miller R.S., Harstad K., Bellan J., Evaluation of equilibrium and non-equilibrium evaporation models for many-droplet gas-liquid flow simulations, International Journal of Multiphase Flow, 24 (1998) 1025-1055.

[17] Kolaitis D.I., Founti M.A., A comparative study of numerical models for Eulerian-Lagrangian simulations of turbulent evaporating sprays, International Journal of Heat and Fluid Flow, 27 (2006) 424-435.

[18] Sazhin S.S., Kristyadi T., Abdelghaffar W.A., Heikal M.R., Models for fuel droplet heating and evaporation: Comparative analysis, Fuel, 85 (2006) 1613-1630.

[19] Zhifu Z., Guoxiang W., Bin C., Liejin G., Yueshe W., Evaluation of Evaporation Models for Single Moving Droplet with a High Evaporation Rate, Powder Technology, 240 (2013) 95-102.

[20] Law C.K., Multicomponent droplet combustion with rapid internal mixing, Combustion and Flame, 26 (1976) 219-233.

[21] Renksizbulut M., Bussmann M., Li X., Droplet vaporization model for spray calculations, Particle & Particle Systems Characterization, 9 (1992) 59-65.

[22] Varanasi K.K., Clack H.L., Miller R.S., On preferential diffusion of binary component liquid droplets evaporating in a two-phase mixing layer, International Journal of Multiphase Flow, 30 (2004) 1235-1257.

[23] Law C.K., Internal boiling and superheating in vaporizing multicomponent droplets, AIChE Journal, 24 (1978) 626-632.

[24] Kneer R., Schneider M., Noll B., Wittig S., Diffusion controlled evaporation of a multicomponent droplet: theoretical studies on the importance of variable liquid properties, International Journal of Heat and Mass Transfer, 36 (1993) 2403-2415.

[25] Torres D.J., O'Rourke P.J., Amsden A.A., Efficient multicomponent fuel algorithm, Combustion Theory and Modelling, 7 (2003) 67-86.

[26] Brenn G., Concentration fields in evaporating droplets, International Journal of Heat and Mass Transfer, 48 (2005) 395-402.

[27] Renksizbulut M., Haywood R.J., Transient droplet evaporation with variable properties and internal circulation at intermediate Reynolds numbers, International Journal of Multiphase Flow, 14 (1988) 189-202.

[28] Haywood R.J., Nafziger R., Renksizbulut M., Detailed examination of gas and liquid phase transient processes in convective droplet evaporation, Journal of Heat Transfer, 111 (1989) 495-502.

[29] Chiang C.H., Raju M.S., Sirignano W.A., Numerical analysis of convecting, vaporizing fuel droplet with variable properties, International Journal of Heat and Mass Transfer, 35 (1992) 1307-1324.

[30] Megaridis C.M., Comparison between experimental measurements and numerical predictions of internal temperature distributions of a droplet vaporizing under high-temperature convective conditions, Combustion and Flame, 93 (1993) 287-302.

[31] Shih A.T., Megaridis C.M., Suspended droplet evaporation modeling in a laminar convective environment, Combustion and Flame, 102 (1995) 256-270.

[32] Shih A.T., Megaridis C.M., Thermocapillary flow effects on convective droplet evaporation, International Journal of Heat and Mass Transfer, 39 (1996) 247-257.

[33] Abou Al-Sood M.M., Birouk M., A numerical study of the effect of turbulence on mass transfer from a single fuel droplet evaporating in a hot convective flow, International Journal of Thermal Sciences, 46 (2007) 779-789.

560 [34] Raghuram S., Raghavan V., Pope D.N., Gogos G., Two-phase modeling of evaporation
561 characteristics of blended methanol–ethanol droplets, International Journal of Multiphase Flow,
562 52 (2013) 46-59.

563 [35] Megaridis C.M., Sirignano W.A., Numerical modeling of a vaporizing multicomponent
564 droplet, Symposium (International) on Combustion, 23 (1990) 1413-1421.

565 [36] Megaridis C.M., Sirignano W.A., Multicomponent droplet vaporization in a laminar
566 convective environment, Combustion science and technology, 87 (1992) 27-44.

567 [37] Megaridis C.M., Liquid-Phase Variable Property Effects in Multicomponent Droplet
568 Convective Evaporation, Combustion Science and Technology, 92 (1993) 291 - 311.

569 [38] Renksizbulut M., Bussmann M., Multicomponent droplet evaporation at intermediate
570 Reynolds numbers, International Journal of Heat and Mass Transfer, 36 (1993) 2827-2835.

571 [39] Zhang H., Evaporation of a suspended droplet in forced convective high-pressure
572 environments, Combustion Science and Technology, 175 (2003) 2237-2268.

573 [40] Haywood R.J., Renksizbulut M., Raithby G.D., Transient deformation and evaporation of
574 droplets at intermediate Reynolds numbers, International Journal of Heat and Mass Transfer, 37
575 (1994) 1401-1409.

576 [41] Schlottke J., Weigand B., Direct numerical simulation of evaporating droplets, Journal of
577 Computational Physics, 227 (2008) 5215-5237.

578 [42] Strotos G., Gavaises M., Theodorakakos A., Bergeles G., Numerical investigation of the
579 evaporation of two-component droplets, Fuel, 90 (2011) 1492-1507.

580 [43] Banerjee R., Numerical investigation of evaporation of a single ethanol/iso-octane droplet,
581 Fuel, 107 (2013) 724-739.

582 [44] Ghata N., Shaw B.D., Computational modeling of the effects of support fibers on
583 evaporation of fiber-supported droplets in reduced gravity, International Journal of Heat and
584 Mass Transfer, 77 (2014) 22-36.

585 [45] Malgarinos I., Nikolopoulos N., Marengo M., Antonini C., Gavaises M., VOF simulations
586 of the contact angle dynamics during the drop spreading: Standard models and a new wetting
587 force model, Advances in Colloid and Interface Science, 212 (2014) 1-20.

588 [46] Malgarinos I., Nikolopoulos N., Gavaises M., Coupling a local adaptive grid refinement
589 technique with an interface sharpening scheme for the simulation of two-phase flow and free-
590 surface flows using VOF methodology, Journal of Computational Physics, 300 (2015) 732-753.

591 [47] Strotos G., Malgarinos I., Nikolopoulos N., Papadopoulos K., Theodorakakos A., Gavaises
592 M., Performance of VOF methodology in predicting the deformation and breakup of
593 impulsively accelerated droplets in: 13th ICLASS, Tainan, Taiwan, 2015.

594 [48] Hirt C.W., Nichols B.D., Volume of Fluid (Vof) Method for the Dynamics of Free
595 Boundaries, Journal of Computational Physics, 39 (1981) 201-225.

596 [49] Brackbill J.U., Kothe D.B., Zemach C., A continuum method for modeling surface tension,
597 Journal of Computational Physics, 100 (1992) 335-354.

598 [50] Lafaurie B., Nardone C., Scardovelli R., Zaleski S., Zanetti G., Modelling Merging and
599 Fragmentation in Multiphase Flows with SURFER, Journal of Computational Physics, 113
600 (1994) 134-147.

601 [51] Perry R.H., Green D.W., Perry's Chemical Engineers' Handbook, 7th ed., McGraw-Hill,
602 1997.

603 [52] Poling B.E., Prausnitz J.M., O'Connell J.P., Properties of Gases and Liquids (5th Edition),
604 in, McGraw-Hill, 2001.

605 [53] Youngs D.L., Time-Dependent Multi-Material Flow with Large Fluid Distortion, in:
606 Morton K.W., Baines M.J. (Eds.) Numerical Methods for Fluid Dynamics,, Academic Press,
607 New York, 1982.

608 [54] Barth T., Jespersen D., The design and application of upwind schemes on unstructured
609 meshes, in: 27th Aerospace Sciences Meeting, American Institute of Aeronautics and
610 Astronautics, 1989.

611 [55] ANSYS®FLUENT, Release 14.5, Theory Guide, in, 2012.

612 [56] Issa R.I., Solution of implicitly discretised fluid flow equations by operator-splitting,
613 Journal of Computational Physics, 62 (1986) 40-65.

614 [57] Hu H., Larson R.G., Evaporation of a sessile droplet on a substrate, Journal of Physical
615 Chemistry B, 106 (2002) 1334-1344.

[58] Mollaret R., Sefiane K., Christy J.R.E., Veyret D., Experimental and numerical investigation of the evaporation into air of a drop on a heated surface, Chemical Engineering Research & Design, 82 (2004) 471-480.

[59] Daïf A., Bouaziz M., Chesneau X., Ali Cherif A., Comparison of multicomponent fuel droplet vaporization experiments in forced convection with the Sirignano model, Experimental Thermal and Fluid Science, 18 (1999) 282-290.

[60] Wong S.C., Lin A.C., Internal temperature distributions of droplets vaporizing in high-temperature convective flows, Journal of Fluid Mechanics, 237 (1992) 671-687.

[61] Nomura H., Ujiie Y., Rath H.J., Sato J.I., Kono M., Experimental study on high-pressure droplet evaporation using microgravity conditions, in: Symposium (International) on Combustion, 1996, pp. 1267-1273.

[62] Theodorakakos A., Bergeles G., Simulation of sharp gas–liquid interface using VOF method and adaptive grid local refinement around the interface, International Journal for Numerical Methods in Fluids, 45 (2004) 421-439.

[63] Zeng Y., Lee C.F., A model for multicomponent spray vaporization in a high-pressure and high-temperature environment, Journal of Engineering for Gas Turbines and Power, 124 (2002) 717-724.

[64] Ozturk A., Cetegen B.M., Modeling of plasma assisted formation of precipitates in zirconium containing liquid precursor droplets, Materials Science and Engineering A, 384 (2004) 331-351.

[65] Strotos G., Gavaises M., Theodorakakos A., Bergeles G., Evaporation of a suspended multicomponent droplet under convective conditions, in: ICHMT, Marrakech, Morocco, 2008.

[66] Taneda S., Experimental Investigation of the Wake behind a Sphere at Low Reynolds Numbers, J. Phys. Soc. Japan, 11 (1956) 1104-1108.

[67] Amani E., Nobari M.R.H., A calibrated evaporation model for the numerical study of evaporation delay in liquid fuel sprays, International Journal of Heat and Mass Transfer, 56 (2013) 45-58.

[68] Tonini S., Cossali G.E., A novel vaporisation model for a single-component drop in high temperature air streams, International Journal of Thermal Sciences, 75 (2014) 194-203.

[69] Abramzon B., Sazhin S., Convective vaporization of a fuel droplet with thermal radiation absorption, Fuel, 85 (2006) 32-46.

[70] Feng Z.-G., Michaelides E.E., Heat and mass transfer coefficients of viscous spheres, International journal of heat and mass transfer, 44 (2001) 4445-4454.

[71] Harvie D.J.E., Davidson M.R., Rudman M., An analysis of parasitic current generation in Volume of Fluid simulations, Applied Mathematical Modelling, 30 (2006) 1056-1066.

[72] Francois M.M., Cummins S.J., Dendy E.D., Kothe D.B., Sicilian J.M., Williams M.W., A balanced-force algorithm for continuous and sharp interfacial surface tension models within a volume tracking framework, Journal of Computational Physics, 213 (2006) 141-173.

[73] Bohacek J., Surface Tension Model for High Viscosity Ratios Implemented in VOF Model, in: ILASS - Europe, Brno, Czech Republic, 2010.

[74] Strotos G., Malgarinos I., Nikolopoulos N., Gavaises M., Numerical investigation of aerodynamic droplet breakup in a high temperature gas environment, Fuel, 181 (2016) 450-462.